Facile fabrication and formation mechanism of aluminum nanowire arrays

Nathan T Nesbitt[1]**, Michael J Burns and Michael J Naughton**

Department of Physics, Boston College, Chestnut Hill, MA 02467, United States of America

E-mail: nathan.nesbitt@gmail.com and naughton@bc.edu

Abstract

Anodized alumina membranes (AAMs) have proven effective at making vertically-oriented and well-ordered metal nanowire arrays, which are useful in plasmonics and electrochemistry. Here, we produced Al nanowires via directed AAM pore nucleation: a patterned oxide mask on a flat Al surface directed where pores did and did not form, the pores acting to oxidize Al around the sites without pores. This left Al nanowires embedded in the AAM, and produced freestanding Al nanowires after etching the AAM. The nanowire tops had two distinct contours, smooth bowls and flat rough surfaces—suggesting that nanowires with bowl tops result from slow pore development relative to pattern-nucleated pores, not pore blockage as prior literature suggests. The observed low porosity of ~2%, as opposed to the more typical 10%, suggests pore nucleation in the electrolyte employed may need greater local variations in electric field or pH, possibly explaining the electrolyte's peculiar ability to make Al nanowires. Finally, a soft nano-imprint lithography process was developed here to pattern the mask without damaging the stamp, avoiding a stamp degradation problem in previous work that utilized hard nano-imprint lithography.

Supplementary material for this article is available online

Keywords: AAO, nano-imprint lithography, metal nanowire array, anodization

(Some figures may appear in colour only in the online journal)

1. Introduction

Anodized alumina membranes (AAMs) have been demonstrated to be useful for the processes to fabricate vertically-oriented and well-ordered arrays of high aspect-ratio metal nanowires over large areas [1]. Nanowires here are defined as pillars having a diameter below 1 μm, vertically-oriented implies the wires' length is perpendicular to the surface they are fixed to, and high aspect-ratio implies height/diameter above ~5. The AAMs are composed of an alumina membrane with a hexagonal array of pores that penetrate it, and are formed by anodizing an aluminum (Al) surface in an electrochemical cell. For nanowire array pitches (i.e. nanowire spacing) above a few micrometers, anodization is used to etch away Al to yield Al nanowires [2]; for pitches below a few micrometers, the pores in the AAM provide a template that is filled with metal [3].

Such metal nanowire arrays have broad utility, as shown in the following examples. Since metal nanowires can act as plasmonic waveguides [4], a sub-diffraction-limited optical microscope was recently proposed and simulated [5]; fabrication of such a device could be realized by modifying an array of metal nanowires. Super-capacitors, which can provide useful energy storage, can be realized by coating a metal nanowire array with a dielectric layer and subsequent metal layer. The high surface area of the nanowire array provides high capacitance, while the ordered structure can ensure direct paths for charge collection; similar devices have shown promising results [6, 7]. In electrochemistry, the high surface area offered by a nanowire array electrode reduces local current density and reaction overpotential, thereby increasing the energy efficiency of electrolyzers and fuel cells [8, 9]. In batteries that depend on intercalation or alloying, such as the popular Li-ion rocking-chair design, some anode materials, such as Al, experience large volume expansion upon Li-ion
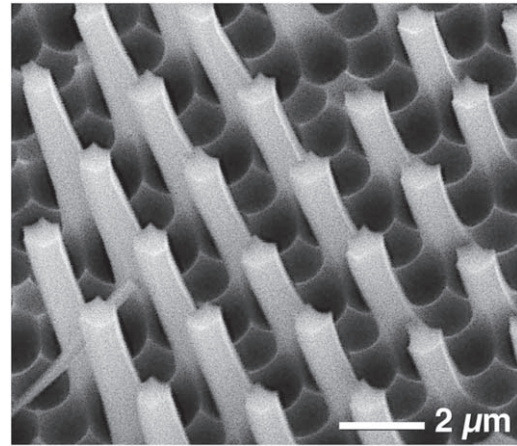
---

1 Author to whom any correspondence should be addressed.

uptake, which can pulverize the electrode during charge-discharge cycles. The small width of nanowires, and the empty surrounding volume, can allow for expansion of the metal with less damage [10]. In each of these examples there will be an array pitch and nanowire height and diameter that optimizes performance. This work thus seeks to improve upon metal nanowire array fabrication processes to expand this tunability.

For AAM formation, an Al surface must be anodized with an electrolyte and applied voltage appropriate for the desired pore array pitch. For pitches between 20 and 400 nm, pores have been shown to form through self-assembly [11], and such self-assembly has shown quasi-ordered hexagonal arrays of pores. In an effort to produce well-ordered arrays, it was shown that patterning an Al surface with a well-ordered array of indents would direct pores to nucleate at the indents [12]. In that work, the indents were made using hard nano-imprint lithography (hard-NIL): pressing a hard silicon carbide stamp with an array of pillars against the Al surface. Subsequently, by using this patterning process, and proper potentials and electrolytes, AAMs with pitch above 400 nm, as high as 2 μm, have been reported [13, 14]. Such patterning appears necessary for pores to nucleate at these large pitch values: for example, for anodization for 1.2 μm pitch, a flat alumina film was observed outside of patterned areas, and pores were only observed within patterned areas [2]. Furthermore, the same work found that within a patterned area, which had a hexagonal array of indents, if the array of indents included a super-array of missing indents, pores would sometimes also not form at the missing indent sites. Thus, if such a missing indent site was surrounded by pores, then when the alumina of the AAM was etched away, an Al nanowire would be left at the site of the missing indent. This contrasts with the findings for AAMs patterned with pitches of 200 and 300 nm, where similar missing indent sites still had pores form [15, 16]. Such pore formation was dubbed a 'self-healing' effect of those AAM fabrication processes, since it allowed AAM fabrication even if a stamp was defected by a few missing pillars.

The above process of Al nanowire array fabrication allowed for lithographically-ordered and vertically-oriented metal nanowire arrays with pitch over 2 μm, which had not before been demonstrated for nanowires made of metal. However, nanowire arrays were only shown over approximately 10 × 10 μm^2 areas, and the hard stamp used to imprint the Al surface was expensive to fabricate (requiring electron beam lithography) and was easily damaged in the stamping process. The 'self-healing' effect was sometimes observed, causing pores to form where nanowires were desired, and thereby nanowires to be missing from arrays. An improved process that would allow for larger and more uniform arrays, without damaging the stamps, is thus desirable. Towards achieving such an improvement, it would be helpful to understand the mechanism of nanowire fabrication, namely, to clarify the root cause of the 'self-healing' effect.

Here, we report a soft nano-imprint lithography (soft-NIL) [17, 18] process to produce Al nanowire arrays via directed-nucleation of AAM pores. Through a series of steps described below, this process imprinted a soft polymer layer using a soft polymer stamp, and transferred that pattern to an oxide mask on the Al surface through a series of etches. The soft polymer stamps showed little damage after imprinting, and were themselves easily and cheaply made from an expensive hard stamp master, thereby protecting the hard stamp from damage. This avoided the expense and inconvenience of stamp degradation found with the hard-NIL process, while still producing comparable well-ordered Al nanowire arrays over approximately 10 × 10 μm^2 areas, as shown in figure 1.

Figure 1. Well-ordered Al nanowire array produced via soft-NIL process.

In addition to improved ease of fabrication, the above masking process resulted in variations in the nanowire topography that offered insights into the physics of the 'self-healing' effect. As discussed below, for anodization at 1.2 μm pitch, it appears that pore nucleation can be either blocked or retarded at sites of missing indents. Further, SEMs showed these AAMs have a porosity of ~2%, as opposed to the 10% that is typical for mild anodization (MA) conditions (viz., 5–10 mA cm^{-2} current density and pitch/voltage of 2.5 nm V^{-1}) [19]. This low porosity suggests large pitch AAMs may require greater local variations in the anodization environment at pore sites to drive pore nucleation, such as higher local electric field or lower local pH. The necessity of greater local variation in electric field or pH could explain why pore nucleation can be slowed or stopped for large pitch anodization (1.2 μm) but not smaller pitch (200 or 300 nm pitch).

2. Experimental

The soft-NIL process employed here ultimately patterns an alumina mask on flat Al. This mask is made of a 400 nm thick alumina film deposited by atomic layer deposition (ALD) onto electropolished Al. Figure 2(a) shows a cartoon of the soft-NIL stamping, pattern transfer, Al anodization, and Al exposure steps for Al nanowire array fabrication.
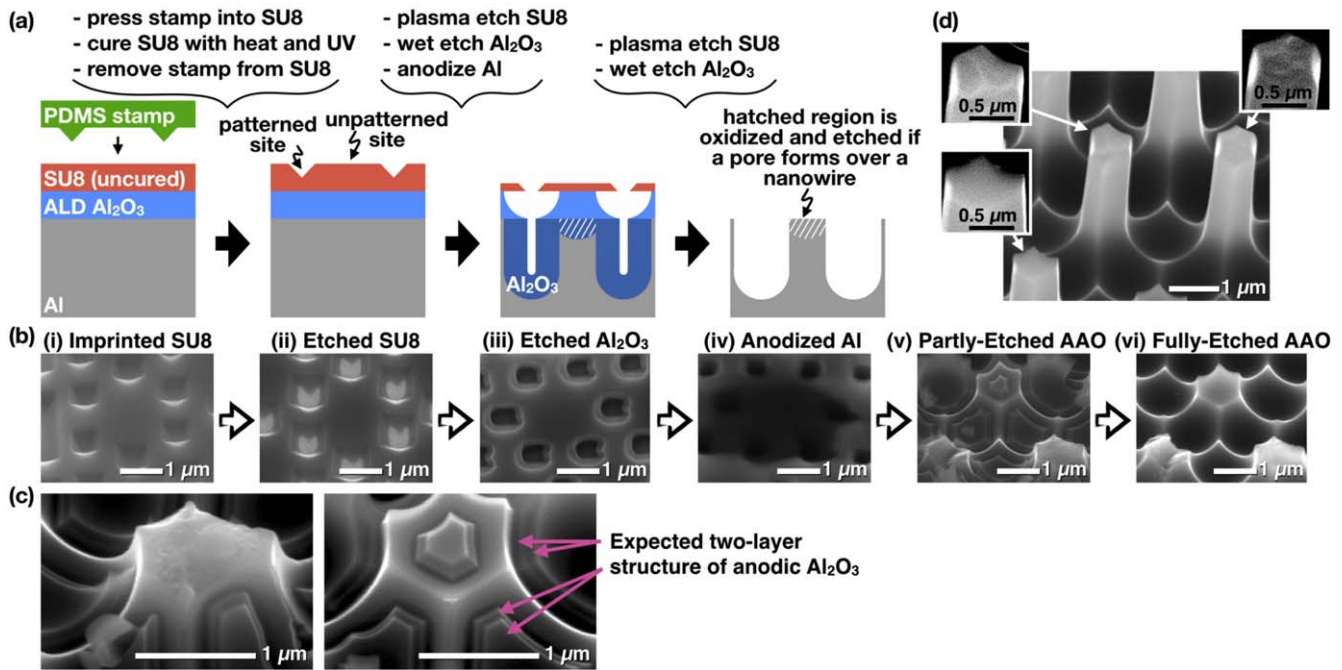
Figure 2. Soft-NIL process for Al nanowire fabrication. (a) Cartoon of the process for patterning a SU-8 photoresist film (MicroChem) with a soft polydimethylsiloxane (PDMS) stamp, transferring the pattern into an alumina mask, anodizing the Al, and etching everything besides Al to expose metal nanowires. Hatched lines indicate anodized alumina that would result in the case that a pore forms over a nanowire, at an unpatterned site. (b) Representative SEMs showing the result of the indicated fabrication steps; very short nanowires allow comparison of nanowire tops, the scalloped bottom, and the anodized alumina layer. (c) Magnified views of the partially-etched AAO, showing the expected two layers of anodic alumina around (left) a rough-topped nanowire and (right) a smooth-topped nanowire. (d) SEM of higher aspect ratio nanowires; two small pores are seen over the center-left nanowire, a single pore over the bottom-left nanowire, and a rough surface over the center-right nanowire. The insets shows a magnified and high contrast view of these nanowire tops.

2.1. Stamp fabrication

Polydimethylsiloxane (PDMS) stamps were prepared in the following process. A Si chip with a $\langle 100 \rangle$ surface orientation was patterned to produce a master from which the PDMS mold was made. The Si chip was sputter coated by 50 nm of Cr (AJA International sputtering system). Before spin-coating with poly(methyl methacrylate) (PMMA), the chip was sequentially rinsed in acetone, isopropanol, deionized water, dried in a N_2 stream, and further dried on a hotplate at 200 °C for $\geqslant 5$ min. From the hotplate, the chip was moved to the spinner (Laurell WS-400E) and a 180 nm PMMA film was spun on (acceleration step: 5 s, 550 rpm s^{-1}, 500 rpm; spin step: 45 s, 550 rpm s^{-1}, 4000 rpm). Before spinning, the solution of PMMA solids (Microchem 495 PMMA A4) was filtered through a 0.45 μm Nylon Acrodisk (Pall Corp.) using a disposable 6 ml syringe. The PMMA was immediately soft baked on a hotplate at 180 °C for 90 s.

Arrays of 300 nm circles were written in the PMMA with an JEOL SEM (probe current $\sim$10 pA, working distance 10 mm, acceleration voltage 30 kV). Arrays were hexagonal with pitch of 1 μm, 1.2 μm, and 1.4 μm. A stretched hexagonal array, with pitch of 1.2 μm except for one direction with a smaller pitch 1 μm, was also included. Each array contained a super-array of missing circles with twice the pitch of the circles. The writing areas were $100 \times 100 \ \mu$m^2 and six patterns of different charge doses were written adjacent to each other, arranged in three columns and two rows. One set of six charge doses was written for each of the four pitches. Note: only the 1.2 μm non-stretched hexagonal pattern showed significant formation of an AAM template, as shown in figure S1, available online at stacks.iop.org/NANO/31/095301/mmedia.

The PMMA was developed for 60 s in (1:3) methyl isobutyl ketone (MIBK): isopropyl alcohol (IPA) (MIBK/IPA 1:3 Developer from MicroChem) and 20 s in IPA (Microchem). The Cr film was etched through the openings in the PMMA for 15 s in Transene Cr Etchant 1020 at 40 °C. The etch was quenched by immersing the chip in a bath of 40 °C deionized water. The chip was rinsed in a deionized water stream and dried in a N_2 stream. The PMMA mask was removed by immersing the chip in acetone for 5 min. The chip was rinsed briefly in a stream of deionized water, and dried in a stream of N_2.

To transfer the pattern from the Cr mask to the Si chip, an aqueous solution of 40%wt potassium hydroxide (KOH) was prepared. KOH pellets were added to a beaker of deionized water, and the solution was raised to 80 °C to facilitate dissolution of the pellets. The solution temperature was then lowered to 40 °C. The solution was stirred at 300 rpm with a 25 mm magnetic stir bar. To etch the exposed Si through the openings in the patterned Cr film, the Si native oxide was removed by immersing the chip in a room temperature buffered oxide etch (BOE from J. T. Baker, 7:1 NH$_4$F:HF) for $\sim$100 s. The chip was rinsed by immersion into two separate baths of deionized water, and then was immersed in the

40 °C, 40%wt, aqueous solution of KOH for ∼300 s. The etch was quenched by immersion in deionized water. The Cr mask was removed by immersing the chip in the Transene Cr Etchant 1020 for ∼4 min. The resulting Si chip master had an array of pyramid shaped depressions where circles had been written in the PMMA by the electron beam. Figure S2 shows SEM images of the Si surface before and after the KOH etch.

To dropcast the PDMS mold from the Si chip master, the Si was placed face-up in a Petri dish (50 mm diameter, 10 mm deep). 4.76 g of Sylgard 184 Silicone Elastomer Base and 0.49 g of Sylgard 184 Silicone Elastomer Curing Agent were mixed and then poured into the Petri dish. The solution was degassed in a vacuum chamber for 10–15 min until bubbles stopped forming. The PDMS was then cured at 75 °C for 2 h. The cured PDMS was peeled away from the Si master, and cut to a convenient size with a scalpel. This PDMS mold had hexagonal arrays of pyramids on it, each with a super-array of missing pyramids at twice the pyramid pitch.

2.2. Aluminum patterning and anodization

Figure 2 shows representative SEMs of the fabrication steps. Al foil pieces cut to $12 \times 6 \times 0.15 \, mm^3$ (Alfa Aesar, ⩾99.99% Al) were flattened in a clamp between two glass microscope slides, rinsed in 3:1 acetone:IPA for 30 s, and then electropolished in 180 ml ethanol + 30 ml 70% perchloric acid (Acros Organics) for 10 min at 10–12 V versus a graphite bar counter electrode. The electrolyte was contained in a $50 \times 90 \, mm$ crystallization dish, and the dish submerged in water in a jacketed beaker, which was cooled to 3 °C by a circulating chiller (Cole-Parmer Polystat 1212202). The electrolyte was stirred at 200 rpm by a 25 mm magnetic stir bar. A 400 nm thick alumina film was deposited by ALD, followed by a 300 nm thick film of SU-8 (MicroChem) negative photoresist. To create a 300 nm thick film, 8.9 mg of SU-8 2002, which has 29.00% solids, was diluted with 23.4 mg of cyclopentatone to make a solution of 8% solids. The diluted SU-8 was spun on (acceleration step: 7 s, 110 rpm s^{-1}, 500 rpm; spin step: 30 s, 550 rpm s^{-1}, 3000 rpm), soft baked on a hotplate at 65 °C for 5 min, followed by 95 °C for 90 s. A PDMS stamp was pressed into the SU-8 with a homemade clamp. The clamp assembly was pre-expose baked at 95 °C for 5 min, the SU-8 was exposed to UV light for 75 s through a window in the clamp assembly, the assembly was post-expose baked at 95 °C for 5 min, and left to cool on a lab bench for 40 min. The sample was removed from the clamp and stamp, the SU-8 exposed again for 75 s, and hard baked (the hotplate was set to 2 min long temperature steps of 65 °C, 95 °C, 120 °C, 150 °C, 180 °C, held at 210 °C for 42 min, stepped back in the reverse order of the up-ramp, turned off, and left to cool to 50 °C before sample removal).

Figure 2(b)-(i) shows scanning electron micrograph (SEM) images of the patterned SU-8 surface. Figure 2(b)-(ii) shows alumina exposed through holes in the SU-8 after etching the SU-8 in a plasma barrel etcher (PVATepla PS-210) for ∼30 s with 150 sccm O_2 + 20 sccm CF_4, 250 W, and the sample on a glass plate inside a Faraday cage; figure S3 shows a low magnification SEM image of the SU-8 mask

after the plasma etch. Figure 2(b)-(iii) shows bowls etched into the alumina film by immersion in ∼20 ml of 1.8%wt chromic acid + 6%wt phosphoric acid on a hotplate at 65 °C for 100 min. An Al etch step was then done, but no change in the sample surface was observed in SEM and it was thus assumed to have had no effect, likely being blocked by an alumina film over the Al. For completeness, though, we include that this etch was done by submersion into Al Etchant (Transene type D) at 25° for 37 s, followed by rinsing in deionized water. Figure 2(b)-(iv) shows the AAM formed after ∼24 h of anodization at 480 V versus a carbon rod counter electrode in 100 ml of 50.5 mM citric acid, 0.287 mM phosphoric acid, 8.71 M (i.e. 50%) ethylene glycol in a beaker immersed in water in a jacketed beaker cooled to 10 °C by a circulating chiller (Cole Parmer Polystat 1212202). Before anodization, the sample was cleaned by sonicating 20 s in IPA and rinsing in a deionized water stream. To begin anodization, the Al electric potential was stepped in 30 s and 10 V intervals from 10 to 80 V and 2 min and 100 V intervals from 180 to 480 V. Figure 2(b)-(v*)* shows the partially etched AAM and the underlying Al surface, exposed by SU-8 removal in the plasma barrel etcher and immersion of the sample into the chromic acid etch described above. Figure 2(b)-(vi*)* shows the exposed Al surface after full removal of alumina. Figure S4 shows photographs of some of the experimental setups used.

3. Results

The soft-NIL process, as described above and shown in the supporting information, was successful in patterning large areas ($200 \times 300 \, \mu m^2$) of a mask on the Al surface, with little damage to the soft stamps. For example, one stamp was used to produce three Al nanowire samples without any apparent stamp degradation; hard stamps of Ni pillars on glass typically showed significant damage after the first or second use (mainly, $100 \times 100 \, \mu m^2$ areas of pillars would often break off of the hard stamp in each use).

To assess the efficacy of the soft-NIL patterning and anodization process on the microscopic scale, we consider the SEMs in figure 2(b). These images focus on an area with short nanowires so the surrounding pores and anodized alumina can also be viewed. Figure 2(b)-(v) shows the Al surface after partial etching of the alumina. The nanowire in the center appears to be below a pore: it has a bowl-shaped top with an alumina film that resembles the alumina at the base of the adjacent pattern-nucleated pores. The nanowire in the bottom-right shows no evidence of pore formation at that site: instead, it has a rough flat surface with no alumina covering it. Since all the alumina present in this image is in the shape of a pore, we assume the alumina from ALD etched faster and has been completely removed. Figure 2(c) shows magnified views of the partially-etched alumina, where the alumina film can be seen to have two layers, as is expected for anodic alumina, which has been shown to have a bottom layer pure Al_2O_3 and a top layer doped by cations from the electrolyte [20, 21]. Figure 2(d) shows a SEM of higher aspect-ratio nanowires:
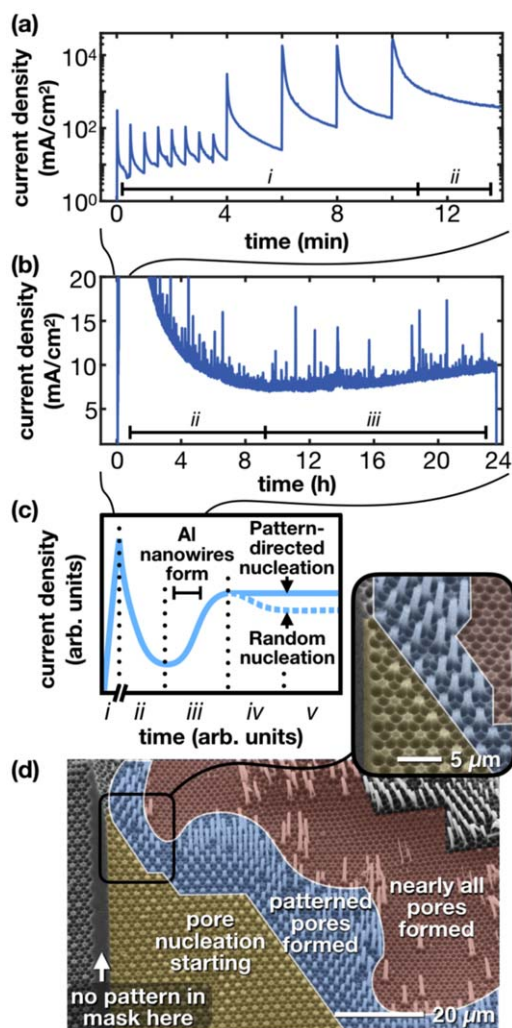
Figure 3. Anodization current density versus time. (a) Stepwise ramp of anodization potential from 0 to 80 V in increments of 30 s and 10 V, and from 80 to 480 V in increments of 2 min and 100 V. (b) Potentiostatic hold at 480 V for 24 h (c) Schematic of a typical *j* versus time to make an AAM: (i) voltage ramp up, (ii) compact barrier oxide growth, (iii) pore nucleation, (iv) merge of excess small pores, (v) steady increase in pore depth [3, 22]; merging of excess pores is not expected for AAMs with pattern-directed nucleation. (d) SEM of Al nanowires after etching away the AAM, showing nanowires present between an area of nucleating pores, and an area with pores at both patterned and unpatterned sites; inset shows magnified view.

the nanowire at center-left (enlarged in top-left inset) appears to have multiple bowl-shapes, suggesting multiple small pores forming at this unpatterned site. Meanwhile, the nanowire at center-right appears to have a flat rough surface (enlarged in the right inset). The nanowire at the bottom-left shows the typical bowl top indicative of a single pore above it (enlarged in bottom-left inset). Figure S5 shows a wide-view SEM of several nanowires embedded in partially etched alumina and showing smooth bowl tops and rough flat tops; the smooth tops appear to have slightly lower height, presumably from anodization and subsequent etching of the aluminum during the retarded pore formation.

The progression of the anodization process can be seen in the current density *j* versus time, shown in figure 3. Figure 3(a) shows *j* while the potential φ is stepped from 0 to 480 V, first in increments of 10 V from minute 0 to 4, and then increments of 100 V from minute 4–14. We correlate the saw-tooth current peaks with the expected capacitive charging of the ionic double layer, and the increasing offset of the baseline of this sawtooth pattern with the expected increasing rate of Al oxidation and Al_2O_3 dissolution at progressively higher potentials.

Figure 3(b) shows *j* while the potential is held constant at 480 V for 24 h. Figure 3(c) shows a schematic of the typical five-stage *j* profile during AAM formation [3, 22]. Following from left to right, *j* first spikes as the potential is ramped up (stage i). When the final potential is reached, *j* drops as the alumina compact barrier oxide increases in thickness, decreasing the electric field in the alumina. This flat alumina layer is understood to form at both surfaces: Al ions (Al^{3+}) from the Al metal migrate through the alumina film to combine with oxygen ions (O^{2-}) at the electrolyte/alumina interface, while O^{2-} from the electrolyte migrate through the film to form alumina at the alumina/Al interface [3, 22, 23]. The electric field across the alumina drives the ion migration, so when the field is lowered, so is the migration of O^{2-} and Al^{3+} (stage ii). *j* reaches a minimum when pores begin to nucleate on the oxide, creating locally thin regions for an increased current to pass through (stage iii). A second peak is reached when pore nucleation has ceased and small pores, which are in excess of the number needed to create a close-packed arrangement of pores, merge together to reduce the density of pores and current (stage iv); note: this second drop in current will not happen for AAMs with pattern-directed pore nucleation, because there should be no excess pores. *j* finally levels off to a constant value that is correlated with a steadily increasing depth of the pores (stage v).

Figure 3(d) shows that the maturity of pore development varies with position on the sample. On the far left, a strip with no pattern in the oxide mask led to no pores in the anodic alumina. Adjacent to this is a region of shallow pores and short Al nanowires, where pore development has evidently progressed slowly, with nucleation still starting. The center of the image has a transition zone where pores only developed significantly at patterned sites, but not at unpatterned sites, producing an array of Al nanowires. On the right side of the image where the pores were deepest (AAM thickest), pores have formed at both the patterned and unpatterned sites, anodizing away the Al nanowires through the 'self-healing' effect of the AAM. However, the presence of a few tall nanowires in this deep area suggests it is possible to make tall Al nanowires in an AAM this thick.

Several studies on the 'self-healing' effect show a trend that smaller pitch AAMs have more complete pore nucleation at unpatterned sites that are adjacent to patterned ones [2, 15, 16]. In all cases, MA was used, defined as anodization at potentials below the potential of dielectric breakdown ($U < U_B$), as opposed to hard anodization (HA) ($U > U_B$) [3]. Porosity here is defined as the percentage of empty area

in a cross-section normal to the pore axis. Anodization in 56 mM oxalic acid (pH $\approx$1.5, $T = 17\,^\circ$C, $U = 80$ V, interpore spacing $D_{int} = 200$ nm, porosity = 7%) showed the 'self-healing' effect, except with only $\sim$3% porosity at unpatterned sites (figure 4(a)) [15]. Anodization in 300 mM phosphoric acid (pH $\approx$ 1.4, $T = 5\,^\circ$C, $U = 120$ V, $D_{int} = 300$ nm, porosity=14%) showed a greater impact on pore formation: unpatterned sites had pores with $\sim$3% of the cross-sectional area of pattern-nucleated pores, and the pattern-nucleated pores were distorted into diamond shapes (figure 4(b)) [16]. Anodization in a solution of 50.5 mM citric acid, 0.287 mM phosphoric acid, 8.71 M (i.e. 50%) ethylene glycol (pH $\approx$ 2.2, $T = 10\,^\circ$C, $j \approx 10$ mA cm^{-2}, $U = 480$ V, $D_{int} = 1200$ nm, porosity = $\sim$2%) showed the greatest impact on pore formation [2]: unpatterned sites showed pores with porosity only 1% or less (figure 4(c)), with nanowires often present underneath these pores. Insets in figure 4(c) show magnified views of the pores, showing the 1% porosity of a unpatterned pore, and 2% porosity of a patterned pore; for comparison, a dashed circle shows what the pore diameter would be for 10% porosity. Figure 4(d) shows a schematic of a vertical cross-section of two pores separated by a nanowire, which is discussed in more detail below. A table of experimental parameters for the three different AAMs above is provided in table 1.

4. Discussion

As mentioned in the introduction, the masking process used here appears to produce two distinct nanowire types, observed in figure 2: (i) some with smooth bowl tops, and (ii) some with rough flat tops. Based on the contour of the Al, the anodic-looking alumina on the smooth bowl-topped nanowire, and the lack of alumina over the rough flat-topped nanowire in the partial-etch of alumina in figure 2(b)-(v), these two nanowire types seem to result from (i) slowly developing pores relative to pattern-nucleated pores, and (ii) full blockage of pore nucleation. The nanowire in figure 2(d) with multiple bowl-shapes does not fall cleanly into one of these categories, but may be partway towards two pores merging into one, as is typical of pore nucleation in AAMs made via self-assembly. In the previous publication on the hard-stamp Al nanowire fabrication process [2], only bowl tops were observed, and it was suggested that pore nucleation was blocked because of a missing indent in the Al. This was apparently incorrect, as the bowl-shape would result from slowly developing pores. The new observations emphasize an interesting result—that an individual pore can be engineered to develop more slowly than the pores surrounding it.

In figure 3(b), the measured j only shows a peak at the conclusion of the voltage ramp, a drop to a minimum, and a gradual increase—it misses the leveling off stage. Thus, the sample apparently has not yet progressed beyond the pore nucleation stage. This is consistent with the SEM in figure 3(d),
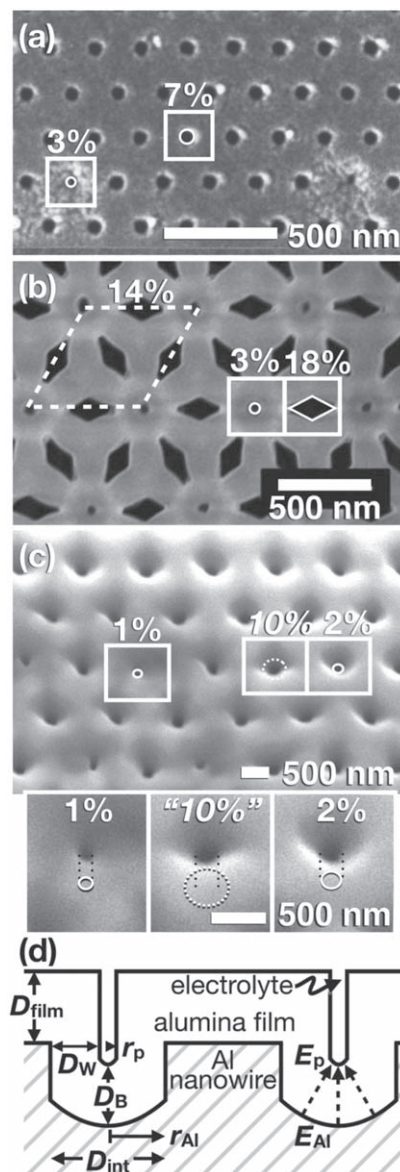
Figure 4. AAMs with unpatterned sites. (a)–(c) SEM images of AAMs following their anodization. Boxes outline the unit cell area, and circles or diamonds the pore area. Above each box is the porosity of the region enclosed. Boxes on the left of each image enclose a pore at an unpatterned site, while those on the right a patterned site. (a) Aqueous oxalic acid, pH 1.5, pitch 200 nm [15]. (b) Aqueous phosphoric acid, pH 1.4, pitch 300 nm [16]. The dashed line rhombus encloses a complete unit cell of the distorted pores. (c) Aqueous phosphoric + citric acid with ethylene glycol, pH 2.2, pitch 1200 nm (image taken at 30° tilt). As a reference, the dotted line shows the pore area for 10% porosity; insets show magnification of highlighted unit cells—pore outlines are offset for easier diameter comparison. (d) Schematic of alumina geometry in an AAM, showing two pores between Al nanowires. Labeled dimensions in left pore are: D_{film} the flat alumina above an Al nanowire, D_W the pore wall thickness, D_B the alumina thickness at the pore bottom, D_{int} the diameter spanning the outer edge of the poor wall (also equal to the AAM pitch), r_{Al} the radius from pore center to the outer edge of the poor wall, and r_p the radius of the pore. Converging field lines at the pore base are shown in the right pore. Panel (a) is reprinted from [15] and (b) is reprinted from [16], with the permission of AIP Publishing.

Table 1. Table showing several important parameters for AAMs in figure 3, panels (a)–(c).

Figures	Interpore spacing (nm)	Voltage (V)	Bulk pH	Temp. (°C)	Porosity (%)	Self-healing
4(a)	200	80	1.5	17	7	Yes
4(b)	300	120	1.4	5	14	Yes
4(c)	1200	480	2.2	10	2	Some

which shows an area on the right where pores developed quickly, but also an area on the left with pore nucleation still starting. In the area on the right where the pattern-directed pores are mature, it is apparently also more likely for a pore to have formed at the site of a nanowire, since few nanowires are present here. The areas with dense nanowires of reasonable height are at the interface of these two regions. Thus, it appears some feature of the well-developed pore area promotes the 'self-healing' effect where pores form at nanowire sites.

To understand the mechanism of the 'self-healing' effect, we consider a mechanical stress model of incipient pore formation [3, 24–29], and then draw a connection between porosity and local variations in electric field and pH. To briefly summarize the model, at a given applied electric potential, an alumina film will grow until its thickness is enough that the potential drop across the film no longer creates sufficient electric field to drive Al^{3+} and O^{2-} ion migration through it (D_{film} in figure 4(d)). When the applied potential is ramped up, the alumina film increases in thickness until it reaches this stable state. This flat film is called a compact barrier oxide. During anodization, anions from the electrolyte are incorporated into the alumina film, causing the film to become less stiff, with different anions causing a different decrease in stiffness [3, 24–27, 29]. Electrostriction due to the potential drop across the alumina applies a compressive force on the film. This can be relieved by roughening the surface, but the surface tension of the film resists this. At a certain potential, the electrostriction will be strong enough to overcome the surface tension, and the film will buckle with a periodicity proportional to the film thickness. This buckled film creates electric field enhancement at the base of incipient pores due to the radially converging electric field lines through the film (similar to field lines shown in figure 4(d)). With the electric field concentrated at the pore base, further oxidation of the Al is confined here. Further nucleation and propagation of pores in the anodic alumina appears to require a balance between continued oxide formation at the alumina/Al interface, flow of this alumina into the pore walls, and dissolution of alumina at the electrolyte/alumina interface via electric field-enhanced dissolution [3, 24–27, 29, 30].

A simple explanation for the retarded nucleation below the oxide mask could be gradual etching of the mask until it is thin enough to start pore development, since this alumina mask starts thicker than the compact barrier oxide for our anodization conditions. Based on the mixture of type i and type ii nanowires, this is likely happening on the masked sample, and evidently at slightly different rates at each nanowire site. Unfortunately, this explanation does not account for how Al nanowires were previously made without the use of a mask (vis., merely indenting the Al without any

mask). Thus, a separate effect must account for slow pore development above type i nanowires while the surrounding pores at patterned sites develop much faster.

Comparison of the geometry of the AAM reported here with those in literature offers insights to this slow pore development. For self-ordered AAMs, a given electrolyte has a potential φ that optimizes how well the pores match an ideal (lowest energy state) hexagonal array [3, 19]. For these optimally-ordered pores, the interpore spacing is twice the barrier oxide thickness D_B at the pore bottom; $D_{int} \approx 2D_B$. The oxide layer dissolves into the electrolyte as it slides laterally from the pore bottom to become the pore wall, with thickness D_W. This defines the pore radius as $r_p = D_B - D_W$. The pore radius thus depends on the rate of chemical alumina dissolution into electrolyte along the pore walls (where no electric field-enhancement would be present). Figure 4(d) shows these variables in a schematic of AAM pores.

As mentioned in the introduction, anodization to produce AAMs can be categorized as mild or hard (MA or HA), and they differ in several ways. One way is the relationship between applied potential φ and the interpore spacing, $D_{int} = k\varphi$, where $k \approx 2.5$ nm V^{-1} for MA, and $k \approx 2.0$ nm V^{-1} for HA [3, 31]. Another is that j for MA is approximately 1–10 mA cm^{-2} and HA approximately 30–250 mA cm^{-2} [3, 31]. Finally, a 10% porosity rule has been empirically shown for optimally-ordered MA [19]. HA has shown lower porosity (viz. 3.3%–3.4% in oxalic acid [31]). Thus, anodization conditions for Al nanowire arrays resemble MA, but have the porosity of HA.

The peculiar low porosity of 1.2 μm pitch AAMs has several connections to alumina dissolution rates. First, purely chemical dissolution of the alumina in the relatively high pH electrolyte, compared to standard AAM electrolytes, should be slow and thereby maintain a small pore radius, r_p. The field-enhanced dissolution [30] begins after a threshold potential is passed, the threshold being lower for electrolytes with lower pH [22]. This means optimally-ordered AAMs with larger pitch, requiring a higher potential φ, are made in higher pH electrolytes. The pore geometry in figure 4(d) shows there is an increase in electric field from the alumina/Al interface to the electrolyte/alumina interface of the pore bottom. This is a function of porosity. Assuming the two interfaces to be concentric sphere segments of respective radii r_p and r_{Al} then the electric field E_p at the electrolyte/alumina interface of the pore base is related to the field E_{Al} at the Al surface by

$$E_p = \left(\frac{r_p}{r_{Al}}\right)^2 E_{Al}, \quad (1)$$

where $r_{Al} = D_{int}/2$. Defining the porosity P in terms of these

radii, $P = \pi r_{\mathrm{p}}^2 / (2r_{\mathrm{Al}})^2$, leads to the pore base field dependence on P,

$$E_{\mathrm{p}} = \frac{\pi}{4P} E_{\mathrm{Al}}. \tag{2}$$

Thus, a decrease in porosity increases the electric field E_{p}, and should drive stronger dissolution of alumina at the pore base.

A similar trend exists for the local variation in pH, resulting from splitting water in the reaction $2\mathrm{Al} + 3\mathrm{H_2O} \rightarrow \mathrm{Al_2O_3} + 6\mathrm{H^+} + 6\mathrm{e^-}$. For a given geometric current density j (the total current divided by the in-plane area), the current density at the pore base j_{p} has an inverse relation to P, $j_{\mathrm{p}} = j/P$. Approximating the steady-state diffusion rate by equating it to the proton flux, J, gives $J = -j/F$, where F is the Faraday constant. Using a simple linear diffusion model for the removal of protons from the alumina/electrolyte interface, the increase in local pH from a decrease in porosity is calculated. Fick's first law of mass diffusion gives the relation $J = -D_0 \Delta c / \Delta x$, where D_0 is the diffusion constant of hydronium in water, Δc the change in proton concentration, and Δx the thickness of the diffusion boundary layer. Thus, the local increase in protons should be

$$\Delta c = \frac{j \Delta x}{D_0 P F}. \tag{3}$$

From figure 3(b), the AAM growth had $j \approx 10\,\mathrm{mA\,cm^{-2}}$. A porosity of $\sim$2% equates to $j_{\mathrm{p}} \approx 500\,\mathrm{mA\,cm^{-2}}$ at the pore bottoms, a five-fold higher value than for 10% porosity. Some of this current is from alumina dissolution and side reactions, but in the approximation that all current is for Al anodization, this corresponds to $5.2 \times 10^{-6}\,\mathrm{mol\,s^{-1}\,cm^{-2}}$ of protons added to the electrolyte. For simplicity, the pH buffering and variation in diffusion constant from the ethylene glycol used in the electrolyte were ignored. With a pH of 2.2, the bulk electrolyte has 6.3 mM of protons. The coefficient of hydronium diffusion D_0 is approximately $9 \times 10^{-7}\,\mathrm{dm^2\,s^{-1}}$ at 25 °C in water of pH 1 or 2 [32]. Setting the diffusion rate J equal to the production rate of protons, the increase in concentration at the alumina/electrolyte interface is found. Assuming a typical diffusion layer thickness of 1 μm gives $\Delta c = 5.76$ mM; a decrease in pH of 0.3 and a doubling of c. Notably, AAM morphology can be sensitive to pH (e.g. a reduction in AAM pitch from 1200 to 1000 nm requires double the acid concentration, a pH reduction of 0.16). Thus, the low $\sim$2% porosity may be due to a greater local decrease in pH required for pore nucleation.

The above results indicate several phenomena that could explain why the 'self-healing' effect is avoided at Al nanowire sites in an AAM. Some approaches to further diminish the 'self-healing' effect and produce a greater yield of Al nanowires in arrays over areas greater than 10×10 μm^2 are the following: if pore nucleation depends heavily on geometric field enhancement, then it will be very sensitive to the radius of curvature of the Al surface. This is consistent with literature [2], which showed that depressions of diameter larger than 400 nm would not produce pores. Thus, indents in Al or holes in a mask that are narrower may better favor pore nucleation at patterned sites over nanowire sites, and mitigate

the 'self-healing' effect. Since ethylene glycol increases the viscosity of the electrolyte, thus slowing hydronium diffusion and increasing the pH gradient, its presence may play an important role in the local variations necessary to form pores in the mildly acidic electrolyte. This suggests that increasing the ethylene glycol concentration and lowering the acidity in electrolytes may mitigate the 'self-healing' effect by confining sufficiently low pH to pattern-directed pores. The ability of the electrolyte to buffer pH could also be varied, to explore whether a stronger buffer of pH would maintain high pH over nanowire sites. Finally, choosing an electrolyte anion with less impact on the alumina mechanical stability, choosing a stiffer mask that won't dissolve or incorporate such anions, increasing the stirring rate to reduce the diffusion layer thickness and further localize concentration gradients in the electrolyte near pores, executing more careful surface preparation and lithography for more consistent patterning of the Al surface, or ramping up the voltage in smaller steps could all be promising approaches for mitigating the 'self-healing' effect and producing higher yields of Al nanowires.

Besides preventing the 'self-healing' effect that anodizes away Al nanowires, large uniform arrays of Al nanowires require uniform development of the AAM across the patterned areas. However, as observed in figure 3(d), pattern-directed pores tend to develop more in certain regions of the sample under the present preparation process. A possible explanation for this is the flat compact barrier oxide may more easily buckle into the incipient pore shape at some sites with favorable defects. The buckling could put pressure on the adjacent pores to also buckle, thereby driving pore formation. This could slowly propagate from the defect, explaining the gradual transition from areas with thick AAM (i.e. tall nanowires) to areas with pore nucleation still starting. The increased local current density at a mature pore should also lower the local pH, possibly aiding pore nucleation at adjacent pores. Possible improvements in the fabrication could include more careful surface and mask preparation to ensure uniformity, or deliberately including an even spacing of defects in the pattern that might act as initial buckling points, to ensure no region gets ahead of another. Since regions of well-developed or poorly-developed AAM tend to be approximately 20–50 μm across, a spacing of this value might be appropriate for these defects.

5. Conclusions

In conclusion, we have demonstrated a soft-NIL process for patterning a mask on Al to produce an AAM that has an array of Al nanowires embedded at desired locations. The yield is unfortunately low, due to a 'self-healing' effect, where pores form in the AAM at locations where nanowires are desired, despite there being no feature in the pattern to direct pore nucleation. However, 10×10 μm^2 areas, as large as the previous report demonstrated [2], were achieved. The nanowires were found to have not only smooth bowl-shaped tops, but sometimes rough flat tops, making it clear that pore formation was not blocked over the bowl-topped nanowires as

previously claimed, but rather was slowed relative to the adjacent pores, which had nucleated at openings in the patterned mask. SEMs of hard-NIL AAMs showed their porosity to be ∼2%, much lower than the typical 10% for MA, while the anodization was otherwise consistent with MA, namely $j \approx 10 \, \mathrm{mA \, cm^{-2}}$ and $k = 2.5 \, \mathrm{nm \, V^{-1}}$. Through geometry arguments, we showed that the lower porosity correlates to electric field and pH values at the pore that are further from the bulk, local extremes which may be necessary for pore development in this large-pitch mild-electrolyte system. Several suggestions were made for improved Al nanowire fabrication processes that might avoid the 'self-healing' effect and achieve larger arrays of Al nanowires.

Acknowledgments

ORCID iDs

Nathan T Nesbitt ● https://orcid.org/0000-0002-1806-1077
Michael J Burns ● https://orcid.org/0000-0001-9804-405X
Michael J Naughton ● https://orcid.org/0000-0002-6733-2398

References

[1] Nesbitt N T and Naughton M J 2017 *Ind. Eng. Chem. Res.* **56** 10949
[2] Nesbitt N T, Merlo J M, Rose A H, Calm Y M, Kempa K, Burns M J and Naughton M J 2015 *Nano Lett.* **15** 7294
[3] Lee W and Park S-J 2014 *Chem. Rev.* **114** 7487
[4] Ditlbacher H, Hohenau A, Wagner D, Kreibig U, Rogers M, Hofer F, Aussenegg F R and Krenn J R 2005 *Phys. Rev. Lett.* **95** 257403
[5] Rose A H, Wirth B M, Hatem R E, Rashed Ahmed A P, Burns M J, Naughton M J and Kempa K 2014 *Opt. Express* **22** 5228
[6] Banerjee P, Perez I, Henn-Lecordier L, Lee S B and Rubloff G W 2009 *Nat. Nanotechnol.* **4** 292
[7] Liu Z *et al* 2012 *Nat. Commun.* **3** 879
[8] McKone J R, Warren E L, Bierman M J, Boettcher S W, Brunschwig B S, Lewis N S and Gray H B 2011 *Energy Environ. Sci.* **4** 3573
[9] Ma M, Djanashvili K and Smith W A 2016 *Angew. Chem., Int. Ed.* **55** 1
[10] Au M, McWhorter S, Ajo H, Adams T, Zhao Y and Gibbs J 2010 *J. Power Sources* **195** 3333
[11] Martín J, Manzano C V and Martín-González M 2012 *Microporous Mesoporous Mater.* **151** 311
[12] Masuda H, Yamada H, Satoh M, Asoh H, Nakao M and Tamamura T 1997 *Appl. Phys. Lett.* **71** 2770
[13] Leung S-F, Yu M, Lin Q, Kwon K, Ching K-L, Gu L, Yu K and Fan Z 2012 *Nano Lett.* **12** 3682
[14] Lin Q, Hua B, Leung S-F, Duan X and Fan Z 2013 *ACS Nano* **7** 2725
[15] Masuda H, Yotsuya M, Asano M, Nishio K, Nakao M, Yokoo A and Tamamura T 2001 *Appl. Phys. Lett.* **78** 826
[16] Smith J T, Hang Q, Franklin A D, Janes D B and Sands T D 2008 *Appl. Phys. Lett.* **93** 043108
[17] Xia Y and Whitesides G M 1998 *Annu. Rev. Mater. Sci.* **28** 153
[18] Rizal B, Archibald M M, Connolly T, Shepard S, Burns M J, Chiles T C and Naughton M J 2013 *Anal. Chem.* **85** 10040
[19] Nielsch K, Choi J, Schwin K, Wehrspohn R B and Gösele U 2002 *Nano Lett.* **2** 677
[20] Thompson G E and Wood G C 1981 *Nature* **290** 230
[21] Coz F L, Arurault L and Datas L 2010 *Mater. Charact.* **61** 283
[22] Parkhutik V P and Shershulsky V I 1992 *J. Phys. D: Appl. Phys.* **25** 1258
[23] Siejka J and Ortega C 1977 *J. Electrochem. Soc.* **124** 883
[24] Yahalom J and Hoar T P 1970 *Electrochim. Acta* **15** 877
[25] Sato N 1971 *Electrochim. Acta* **16** 1683
[26] Garcia-Vergara S, Skeldon P, Thompson G and Habazaki H 2006 *Electrochim. Acta* **52** 681
[27] Garcia-Vergara S, Hashimoto T, Skeldon P, Thompson G and Habazaki H 2009 *Electrochim. Acta* **54** 3662
[28] Vojkuvka L, Santos A, Pallarès J, Ferré-Borrull J, Marsal L and Celis J 2012 *Surf. Coat. Technol.* **206** 2115
[29] Baron-Wiecheć A, Burke M, Hashimoto T, Liu H, Skeldon P, Thompson G, Habazaki H, Ganem J-J and Vickridge I 2013 *Electrochim. Acta* **113** 302
[30] O'Sullivan J P and Wood G C 1970 *Proc. R. Soc.* A **317** 511
[31] Lee W, Ji R, Gösele U and Nielsch K 2006 *Nat. Mater.* **5** 741
[32] Lee S H and Rasaiah J C 2011 *J. Chem. Phys.* **135** 124505